Applied Mathematical Modelling 157 (2026) 116867

Contents lists available at ScienceDirect

Applied Mathematical Modelling

journal homepage: www.elsevier.com/locate/apm

Sound diffusion properties of triply periodic minimal surfaces using three-dimensional FDTD simulations

David Ramírez-Solana [a,b], Valentino Sangiorgio [c,b], Javier Redondo [c], Muhammad Gulzari [a,*]

[a] Centre for Critical Infrastructure Research, School of Civil Engineering, College of Engineering and Architecture, University College Dublin, Richview Newstead Block B (Main Bld), Dublin, D04 V1W8, Ireland
[b] Department of Engineering and Geology (INGEO), D'Annunzio University of Chieti-Pescara, Viale Pindaro, 42, Pescara, 65127, Italy
[c] Instituto de Investigacion para la Gestion Integrada de Zonas Costeras, Universitat Politecnica de Valencia, C. Paranimf, 1, Gandia, 46730, Spain

ARTICLE INFO

Editor: Johann Sienz

Keywords:
Sound diffuser
Acoustics
Finite-difference time domain (FDTD)
Triply periodic minimal surfaces (TPMS)

ABSTRACT

Triply Periodic Minimal Surfaces (TPMS) have been noticed in various engineering disciplines such as biomechanics, heat transfer, and structural mechanics due to their continuous curvature, high surface-to-volume ratio, and compatibility with additive manufacturing. In acoustics, recent research has explored their absorption and bandgap properties; however, their potential as sound diffusive surfaces remains largely unexplored. Addressing this research gap, the present study investigates the frequency-dependent sound diffusion performance of six TPMS geometries using three-dimensional Finite-Difference Time-Domain (FDTD) simulations. The analysis follows the ISO 17497-2 standard and is performed using two complementary models: a high-fidelity "Big Model" and a fast Near-Field to Far-Field (NFFF) approximation. Results show that certain TPMS, such as Costa and Scherk's Tower, achieve enhanced diffusion at mid-to-high frequencies, while others like Batwing exhibit tunable low-frequency peaks. The absence or presence of a rigid backing is shown to significantly influence diffusive behavior. Despite the reduced computational complexity of the NFFF model, its predictions closely match the full model, enabling efficient parametric studies. Finally, potential application of TPMS are discussed, such as the integration of TPMS-based surfaces into acoustic partition panels for improving speech intelligibility in open-plan spaces.

1. Introduction

In the past five decades, since Schroeder's pioneering work on sound diffusers in 1975 [1], these devices have proven their effectiveness in increasing spatial sound diffuseness, mitigating flutter echoes, and minimizing coloration phenomena [2]. Over the years, numerous alternatives to Schroeder's original designs have been proposed: from the use of different numerical sequences to shape the depth profiles [3], to replacing stepped geometries with more organic or visually appealing forms [4], or even by using irregular patterns of reflective and absorptive patches [5]. A key limitation of classical phase diffusers, those composed of arrays of wells with varying depths, is that the lowest frequency at which significant diffusion occurs is governed by the maximum wall depth. To achieve effective diffusion in the low-frequency range i.e., the 125 Hz and 250 Hz octave bands, such structures typically require depths close to 1 m.

* Corresponding author.
E-mail addresses: david.ramirezsolana@ucd.ie (D. Ramírez-Solana), muhammad.gulzari@ucd.ie (M. Gulzari).

https://doi.org/10.1016/j.apm.2026.116867
Received 25 July 2025; Received in revised form 28 December 2025; Accepted 23 February 2026
Available online 1 March 2026
0307-904X/© 2026 The Author(s). Published by Elsevier Inc. This is an open access article under the CC BY license (http://creativecommons.org/licenses/by/4.0/).

In an effort to overcome this limitation, various recent approaches have explored the use of sonic crystals and acoustic metamaterials[6–9]. Nevertheless, the field of acoustic diffuser design has progressed at a comparatively slower pace than other branches of acoustics. Although the benefits of QRD (Quadratic Residue Diffuser) [10,11] and Schroeder sequence-based [4] diffusers are well established, recent advances in diffuser geometry and functionality have been modest. For instance, between the introduction of curved diffusers in the late 1990s [3] and more recent developments such as those by Ballesteros et al.[12] and Brandão et al.[13], no major breakthroughs in diffuser design have occurred, apart from the use of Sonic Crystals [6,14], metadiffusers [8] and spiral ones [15]. Furthermore, It is also worth highlighting the improved architectural integration of diffusers during this period [9,16], along with gradual gains in their overall efficiency.

On the other hand, although the first studies on new periodic minimal surfaces date back to the 1970s for use as lightweight structural materials [17], recent research has focused on Triply Periodic Minimal Surfaces (TPMS) manufactured through 3D-printing, highlighting them as promising alternatives to conventional geometries in architectural acoustics [18]. These surfaces, characterized by zero mean curvature and smooth, continuous topologies, are especially well-suited for additive manufacturing and exhibit a range of advantageous physical behaviors[19–22]. Their use has garnered traction across multiple engineering disciplines including biomechanics[23,24], heat transfer [25], and structural mechanics [26–28], and more recently, acoustics[29–34]. Their smooth geometric continuity enables efficient 3D-printing and provides acoustic behaviors that are just beginning to be explored.

Studies conducted in recent years have shown promising results regarding the acoustic response of TPMS. For example, Guo et al.[31] demonstrated topological properties TPMS-based crystals and Guan et al.[30] conducted experiments on TPMS geometries to evaluate their sound absorption capabilities. However, there remains a clear gap in the literature concerning the diffusion performance of these structures, an essential property in the design of acoustically optimized spaces. The main contribution of this study is to provide clear information about the acoustic diffusion properties of some of the most common TPMS. In this way, when choosing one of the TPMS designs for integration into indoor partitions or wall installations, selection can be guided by their diffusion properties, in addition to other already well-studied criteria such as aesthetics, thermal and mechanical properties.

The remainder of this paper is organized as follows. Section 2 describes the implementation of the three-dimensional (3D) Finite-Difference Time-Domain (FDTD) method used to model sound wave propagation and interaction with complex surfaces. Section 3 introduces the six selected TPMS, including their implicit or parametric definitions. Section 4 outlines the methodology, including the two simulation models based on ISO 17497-2: a high-resolution "Big Model" and a computationally efficient Near-Field to Far-Field (NFFF) transformation model. Section 5 presents the numerical results, comparing the diffusion performance of all TPMS and analyzing their best and worst frequency responses. Section 6 proposes potential architectural applications for these geometries as acoustic partition panels, particularly in office environments. Finally, Section 7 concludes the study with suggestions and recommendations for future research.

2. Three-dimensional (3D) finite-difference time-domain (FDTD) simulation technique

The FDTD method is a powerful computational technique used to solve wave equations in acoustics [35,36]. It involves discretizing the time and space domains to simulate the propagation of sound waves through different media. FDTD is particularly useful for modeling the interaction of sound with complex structures, making it an essential tool for this research. This work employs three-dimensional FDTD simulation to analyze and optimize the diffusion properties of periodic acoustic structures such as the TPMS. In this section, the steps followed for the implementation of the FDTD simulation method are described, adapting the two-dimensional FDTD model used, as previously reported by J. Redondo et al.[37]:

The equations for momentum conservation and continuity provide the basis for an acoustic FDTD model without any sound sources. These models may be expressed as follows in a homogeneous medium with no losses:

$$\frac{\partial p}{\partial t} + \mathcal{B}\vec{\nabla}\cdot\vec{u} = 0, \tag{1}$$

$$\vec{\nabla} p + \rho_0 \frac{\partial \vec{u}}{\partial t} = 0, \tag{2}$$

where $\vec{u} = (u_x, u_y, u_z)$ is the vector denoting the particle velocity field, p represents the pressure field, ρ_0 stands for the mass density of the medium and $\mathcal{B} = \rho_0 c^2$ is the Bulk modulus, where c is the speed of sound in the host medium. The central finite difference technique is used to approximate the spatial and temporal derivatives of pressure and particle velocity.

For the sake of readability and to avoid repeating very similar equations, the variable $\xi = (x, y, z)$ can be used to represent the three spatial coordinates. In this way, the governing equations of FDTD apply to both 2D and 3D cases.

For instance, we can use this technique to estimate the derivative of sound pressure with respect to any spatial coordinate, which can be expressed by the following equation:

$$\left.\frac{\partial p}{\partial \xi}\right|_{\xi=\xi_0} \approx \frac{p\left(\xi_0 + \frac{\Delta\xi}{2}\right) - p\left(\xi_0 - \frac{\Delta\xi}{2}\right)}{\Delta\xi}. \tag{3}$$

In particular, the spatial interval denoted by $\Delta\xi$ represents the distance between closely-spaced points along the ξ-axis. In D dimensions, we must define $D+1$ grids: 1 for pressure and D for the different components of particle velocity. To minimize the influence of higher-order terms in Eqs. (4)–(7), these grids are 'staggered'. For instance, the mesh for the ξ component of particle velocity is shifted by $\Delta\xi/2$ relative to the pressure mesh. The same principle applies to the time intervals, the particle velocity meshes are shifted by $\Delta t/2$ in time compared to the pressure mesh. By adopting this approach, we can derive a set of updated equations that

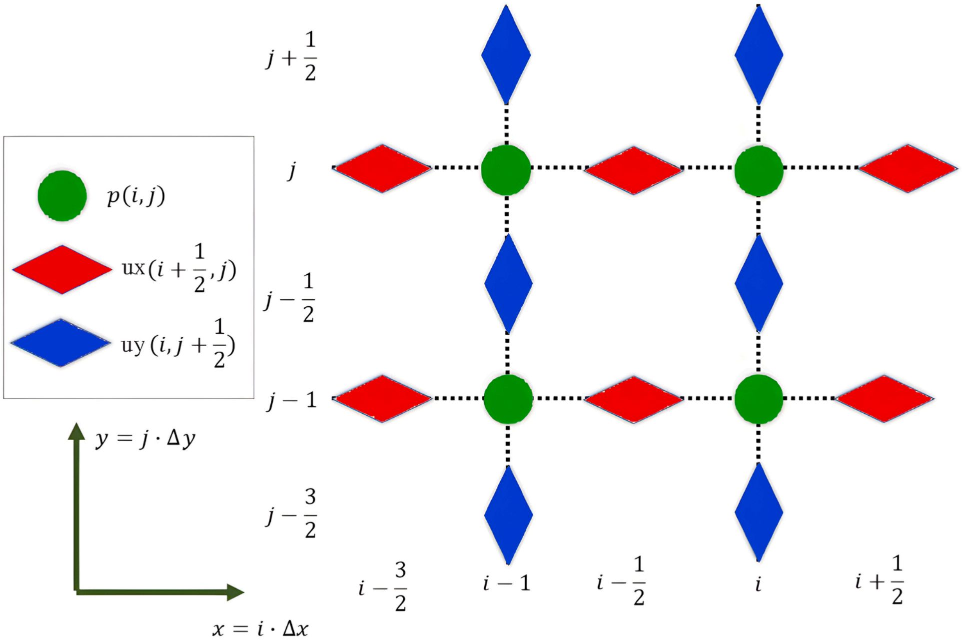

Fig. 1. Two-dimensional FDTD scheme for pressure and particle velocity fields.

allow us to determine the values of pressure and particle velocity after iterating for a specified number of steps. These equations are the following:

$$p^{n+1/2}_{i,j,k} = p^{n-1/2}_{i,j,k} - \mathcal{B}\Delta t\left(\frac{ux^{n}_{i+1/2,j,k} - ux^{n}_{i-1/2,j,k}}{\Delta x} + \frac{uy^{n}_{i,j+1/2,k} - uy^{n}_{i,j-1/2,k}}{\Delta y} + \ldots + \frac{uz^{n}_{i,j,k+1/2} - uz^{n}_{i,j,k-1/2}}{\Delta z}\right) \tag{4}$$

$$ux^{n+1}_{i+1/2,j,k} = ux^{n}_{i+1/2,j,k} - \frac{\Delta t}{\rho}\left(\frac{p^{n+1/2}_{i+1,j,k} - p^{n+1/2}_{i,j,k}}{\Delta x}\right) \tag{5}$$

$$uy^{n+1}_{i,j+1/2,k} = uy^{n}_{i,j+1/2,k} - \frac{\Delta t}{\rho}\left(\frac{p^{n+1/2}_{i,j+1,k} - p^{n+1/2}_{i,j,k}}{\Delta y}\right). \tag{6}$$

$$uz^{n+1}_{i,j,k+1/2} = uz^{n}_{i,j,k+1/2} - \frac{\Delta t}{\rho}\left(\frac{p^{n+1/2}_{i,j,k+1} - p^{n+1/2}_{i,j,k}}{\Delta z}\right). \tag{7}$$

The superscripts denote the time index, and the subscripts denote the spatial indices as follows:

$$p^{n+1/2}_{i,j,k} = p(i\Delta x, j\Delta y, k\Delta z, (n+1/2)\Delta t) \tag{8}$$

$$ux^{n}_{i+1/2,j,k} = u_x((i+1/2)\Delta x, j\Delta y, k\Delta z, n\Delta t) \tag{9}$$

$$uy^{n}_{i,j+1/2,k} = u_y(i\Delta x, (j+1/2)\Delta y, k\Delta z, n\Delta t). \tag{10}$$

$$uz^{n}_{i,j,k+1/2} = u_z(i\Delta x, j\Delta y, (k+1/2)\Delta z, n\Delta t). \tag{11}$$

To have a better understanding of the update equations, Fig. 1 represents the two-dimensional FDTD scheme.

With aim of guaranteeing the numerical convergence, it is important that the time step is sufficiently small to accurately simulate wave propagation. This relationship between the spatial steps and the time step is determined by the Courant-Friedrichs-Levy number s, which can be defined as follows in three dimensions:

$$s = c\Delta t\sqrt{\left(\frac{1}{\Delta x}\right)^2 + \left(\frac{1}{\Delta y}\right)^2 + \left(\frac{1}{\Delta z}\right)^2} \leq 1 \tag{12}$$

Another limitation of the FDTD method is that the maximum allowable element size in the spatial discretization is determined by the highest frequency being simulated. This limitation is shared with other numerical techniques.The standard criterion suggests using at least four elements per wavelength: in the related literature by A. Taflove et al.[36] it is shown that for a high level accuracy a minimum of 10 elements per wavelength is needed. Consequently, at high frequencies, solving the numerical problem becomes computationally intensive. In this work, we employed a spatial step small enough to ensure accurate results up to 5 kHz.

In order to remove unwanted reflections from the boundaries of the computational domain, an absorbing boundary condition is used. The technique, known as "Perfectly Matched Layers" (PML) [38] is chosen. PML introduces a lossy medium near the boundaries, requiring modifications to Eqs. (1) and (2) to incorporate attenuation factors for each dimension considered (denoted as γ_ξ in D dimensions). This adjustment is expressed as follows:

$$\frac{\partial p_\xi}{\partial t} + \gamma_\xi p_\xi + B\left(\frac{\partial u_\xi}{\partial \xi}\right) = 0 \tag{13}$$

$$\frac{\partial p}{\partial \xi} + \rho\left(\frac{\partial u_\xi}{\partial t} + \gamma_\xi u_\xi\right) = 0 \tag{14}$$

In Eqs. (13) and (14) the sound pressure p is divided into D separate components p_ξ being $\xi = (x, y, z)$. These components do not have any physical significance and are defined merely for the purpose of optimizing the sound absorption performance. The actual pressure is the sum of the three components p_x, p_y and p_z.The attenuation factors are set to zero within the integration area but are heightened in regions near the boundaries.

3. Triply periodic minimal surfaces (TPMS)

A TPMS is defined implicitly by a scalar function $f(x, y, z)$. To turn the infinitely thin surface into a 3D volume of thickness t within a periodic lattice of size a, we define the solid domain as:

$$|f(x, y, z)| \le \varepsilon \tag{15}$$

where:

$$\varepsilon = \kappa \cdot \frac{t}{a} \tag{16}$$

with:

- a is the lattice constant, i.e., the periodicity of the unit cell.
- t is the desired thickness of the structure (in the same units as a).
- κ is a scaling factor (typically $\kappa \in [1, 2]$) to adapt the threshold to the functional range of f.

For each TPMS, in Table 1 we express $f(x, y, z)$ using scaled variables $x', y', z' = \frac{2\pi}{a}\,\xi$, with $\xi = (x, y, z)$ as in the previous section, so the surface is periodic over a cubic cell of size $a \times a \times a$.

In this study, we compare six TPMS (Schoen's Batwing [23], Scherk's Tower [39,40], Gyroid [26], Diamond [41], Schwarz Primitive [24], Costa Surface [42,43]), two of which are particularly unique: Scherk's Tower and Costa Surface. Scherk's Tower is periodic in only two axes and replicated along the z-axis, which is why it is referred to as Scherk's Second Surface in its definition for creating the Tower. On the other hand, the Costa surface is an extremely complex surface in mathematical terms, which continues to present a challenge for its parametric definition [44]. The Costa surface does not have a simple trigonometric implicit function. It is generally defined parametrically or numerically via Weierstrass data. For a deeper explanation of the Costa Surface equation and Weierstrass functions ($\wp, \zeta$), the reader is referred to Appendix A.

4. Methodology

4.1. FDTD simulations and near-to-far field transformation

To evaluate the time-domain acoustic behaviour of the TPMS structures, we conducted three-dimensional simulations using the FDTD method. This volumetric technique enables broadband analysis from a single simulation and provides direct access to the temporal evolution of reflected sound fields [37]. The pressure and particle velocity fields were computed using staggered grids to enhance numerical stability, and the boundaries were treated with PMLs to prevent spurious reflections [45,46].

We used a total-field/scattered-field (TF/SF) formulation to isolate the scattered wave field, which is essential when analyzing time spreading. The incident signal was injected with a plane transparent source[47]. Excitation was performed using Ricker wavelets centered at 250 Hz, 500 Hz, 1 kHz and 2 kHz, ensuring wideband coverage without introducing large-amplitude frequency components near zero frequency (D.C. frequency) which can cause resolution problems in the audible part of the spectrum. These wavelets are widely adopted in geophysical and acoustic applications for their compact temporal support and spectral neutrality [48].

This simulation framework enables the quantification of time spreading, a phenomenon associated with temporal dispersion of reflected energy due to geometric features. Surfaces that promote spatial diffusion also tend to exhibit strong time spreading, as evidenced in prior studies [49,50].

To overcome computational limitations associated with far-field evaluations, we applied a NFFF Transformation. Pressure and velocity values recorded on a closed surface Γ above the TPMS structure (see blue plane in Fig. 3b) were used to reconstruct the

Table 1
TPMS solid domain equations for a cubic unit cell with lattice constant a. The solid domain is defined by $|f(x, y, z)| \leq \kappa \cdot \frac{t}{a}$.

Implicit Equation	TPMS Name	Unit Cell Image
$3\left(\cos\left(\frac{2\pi}{a}x\right)+\cos\left(\frac{2\pi}{a}y\right)+\cos\left(\frac{2\pi}{a}z\right)\right)+10\cos\left(\frac{2\pi}{a}x\right)\cos\left(\frac{2\pi}{a}y\right)\cos\left(\frac{2\pi}{a}z\right)$	Schoen's Batwing	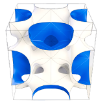
$\sinh\left(\frac{2\pi}{a}x\right)\sinh\left(\frac{2\pi}{a}y\right)-\sin\left(\frac{2\pi}{a}z\right)$	Scherk's Tower	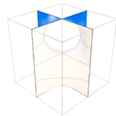
$\cos\left(\frac{2\pi}{a}x\right)\sin\left(\frac{2\pi}{a}y\right)+\cos\left(\frac{2\pi}{a}y\right)\sin\left(\frac{2\pi}{a}z\right)+\cos\left(\frac{2\pi}{a}z\right)\sin\left(\frac{2\pi}{a}x\right)$	Gyroid (Schoen G)	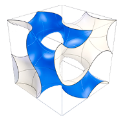
$\begin{aligned}&\sin\left(\frac{2\pi}{a}x\right)\sin\left(\frac{2\pi}{a}y\right)\sin\left(\frac{2\pi}{a}z\right)\\&+\sin\left(\frac{2\pi}{a}x\right)\cos\left(\frac{2\pi}{a}y\right)\cos\left(\frac{2\pi}{a}z\right)\\&+\cos\left(\frac{2\pi}{a}x\right)\sin\left(\frac{2\pi}{a}y\right)\cos\left(\frac{2\pi}{a}z\right)\\&+\cos\left(\frac{2\pi}{a}x\right)\cos\left(\frac{2\pi}{a}y\right)\sin\left(\frac{2\pi}{a}z\right)\end{aligned}$	Diamond (Schwarz D.)	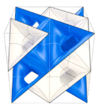
$\cos\left(\frac{2\pi}{a}x\right)+\cos\left(\frac{2\pi}{a}y\right)+\cos\left(\frac{2\pi}{a}z\right)$	Schwarz P.	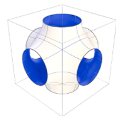
$\begin{aligned}x&=a\,\Re\mathrm{e}\left(\zeta\left(u+\frac{\pi}{4e_1}\right)-\zeta(w)-\frac{1}{2}\zeta\left(w-\frac{i}{2}\right)\right)\\y&=a\,\Re\mathrm{e}\left(\zeta\left(u+\frac{\pi}{4e_1}\right)-\zeta(w)+\frac{1}{2}\zeta\left(w-\frac{i}{2}\right)\right)\\z&=a\sqrt{\frac{c}{e_1}}\ln\left\|\frac{\wp(w)-e_1}{\wp(w)+e_1}\right\|\end{aligned}$	Costa Surface	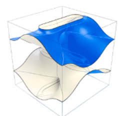

far-field response. In the time-domain formulation, the pressure at a far-field point $\mathbf{r}'$ can be obtained by:

$$p(\mathbf{r}',t)=\frac{1}{4\pi}\int_\Gamma\left[\frac{1}{Rc_0}\frac{\partial}{\partial t}\left(\mathbf{u}(\mathbf{r},t-R/c_0)\cdot\mathbf{n}\right)-\nabla\cdot\left(\frac{\mathbf{n}\,p(\mathbf{r},t-R/c_0)}{R}\right)\right]d\Gamma, \tag{17}$$

where $R=\|\mathbf{r}'-\mathbf{r}\|$, $\mathbf{n}$ is the local outward normal, and c_0 is the speed of sound in air. This procedure, derived from the equivalence theorem, is analogous to those applied in electromagnetic and aeroacoustic applications [51,52].

4.2. Parametric modelling of TPMS-based solids

Using a *Grasshopper* visual script combined with the *Millipede* plugin, we generated TPMS through a customizable three-step process based on isosurface three-dimensional modeling. First, a single TPMS cell was generated as the base unit. Next, the cell was replicated and arranged into a larger periodic structure. Finally, the mesh was thickened and converted into solid geometry for further use.

Step 1: The process begins with the definition of a three-dimensional domain ranging from $-\pi$ to π along the x, y, and z axes using the `Construct Domain` and `Range` components. This domain is discretized into a uniform grid by specifying a resolution parameter through the `ISOResSteps` input, which controls the number of subdivisions along each axis. Mathematical expressions corresponding to canonical TPMS types, such as Schwarz P., Gyroid, Diamond, Scherk's Tower, and Batwing, are embedded as selectable functions.

The `isosurface` component of the *Millipede* plugin converts these mathematical expressions into three-dimensional meshes, enabling the visualization and further manipulation of the resulting TPMS geometries.

Step 2: Once the single TPMS geometry is generated by the `isosurface` component, spatial repetition is achieved using components such as `Domain Box` and `Box Array`, enabling the structure to be replicated along the x, y, and z directions.

Step 3: In the final stage of the script, the mesh is thickened through offsetting operations. A series of mesh-processing components (including `Align Vertices`, `Combine & Clean`, and `SubD`) are applied to refine the geometry and convert it into a clean, closed polysurface suitable for further applications such as fabrication or analysis. Fig. 2 shows, on the top, the mathematical formulations and three-step workflow used for TPMS generation, and on the bottom, an example of a TPMS geometry created using the Box Array component with tiling parameters $x = 1$, $y = 3$, and $y = 3$.

Since the Costa Surface does not have a trigonometric implicit function, as previously discussed, its generation required a different approach. Employing the MATLAB Engine API for Python [53] in combination with available elliptic function scripts [54], the Costa Surface was first computed in MATLAB. Subsequently, it was integrated into the modeling workflow via a Python script that enabled communication with Grasshopper [55]. This integration occurred at ***Step 2*** of the Grasshopper workflow, replacing the isosurface-generation phase used for standard TPMS geometries. From this point onward, the same procedural steps—including spatial arraying and solid generation—were applied to the Costa geometry, enabling seamless integration into the broader parametric design pipeline [55].

4.3. International standard ISO 17497-2

ISO 17497-2 specifies a method for measuring the diffusion coefficient of surface treatments using a three-dimensional goniometric measurement system in an anechoic or semi-anechoic chamber[56]. The setup consists of a rotating loudspeaker and microphone mounted on a mechanical arm or frame that allows them to move independently around a fixed sample in a hemispherical arrangement[57]. Measurements are made at various incident and reflection angles to evaluate how uniformly the surface scatters sound energy compared to a perfectly reflective flat surface. This directional data enables a detailed angular analysis of the reflected field.

The diffusion coefficient (δ) is computed by evaluating the homogeneity of the angular distribution of the reflected sound energy. It can be further normalized by comparison with a flat reference surface. Specifically, it quantifies how evenly sound is scattered in different directions, and it is calculated for each frequency band using the measured impulse responses. The goal of this method is to objectively assess the diffusivity of a surface — that is, its ability to redistribute sound uniformly.

To evaluate the diffusion coefficient, a $3\times3\times1$ structure of the selected TPMS will be placed at the center of a cubic room with PML walls. We will use two three-dimensional FDTD models, both following the procedure outlined in ISO 17497-2. The chosen size of $3\times3\times1$ is necessary because the ISO 17497-2 standard requires three repetitions of the structure in the plane of incidence to be analyzed. The first model will emulate a large anechoic chamber, in which the reflected acoustic pressure values will be measured using the goniometer with the two red arcs. This model is called *Big Model* (see Fig. 3a).

The second model will consist of a smaller box surrounding the TPMS structure, and the NFFF transformation will be performed according to Eq. (17).This second model is called *NFFF* (see Fig. 3b). For the large room simulations, the domain representing the room measures $7.00 \times 7.00 \times 4.20$ meters, with a PML thickness of 0.20 meters. The TPMS diffuser used in the simulation has dimensions of $0.60 \times 0.60 \times 0.20$ meters. The radius of the measurement arcs is set to 3.20 meters. For the NFFF simulations, the domain is a cube with dimensions $1.20 \times 1.20 \times 1.20$ meters, also surrounded by a PML of 0.20 meters thickness. The TPMS diffuser maintains the same dimensions of $0.60 \times 0.60 \times 0.20$ meters. The measurement plane is placed at a distance of 0.05 meters above the top surface of the diffuser. In the simulations called "with backing" a rigid backing is imposed behind the TPMS to emulate a rigid wall where the diffuser would be placed. The computation times on a 12-core Intel i7 processor were as follows: the Big Model required 9.5 hours, while the NFFF model took approximately 3 minutes. This reduction from 9.5 hours to 3 minutes represents a time savings of approximately 98.95%.

5. Results

Due to the large volume of data, this section divides the numerical analysis into two parts: first, a comparison of the TPMS structures using the two different 3D models, and second, an evaluation of their acoustic diffusion performance highlighting optimal and suboptimal frequency ranges.

5.1. Model comparison analysis

Since our TPMS are placed in a square lattice and they can be scaled, we should keep in mind the size of the cubic unit cell and the related wavelength frequency of interest. For a square lattice with a periodicity of $a = 0.2$ m, the Bragg frequency is given by $f_{\text{Bragg}} = \frac{c}{2a} = \frac{343}{0.4} = 857.5$ Hz, assuming the speed of sound in air is $c = 343$ m/s[58]. In addition to showing the diffusion coefficient (δ) normalized with respect to a flat surface, the legend in Figs. 4 and 5 also indicates the average value over the entire frequency range covered by the ISO 17497-2 standard (100–5000 Hz).

In Fig. 4, negative values (below zero) indicate that the diffusion coefficient underperforms relative to a flat surface at that frequency, suggesting the TPMS structure focuses reflections. In terms of average performance (δ_{avg}), all geometries exhibit similar behavior, with values clustering around 0.2. Costa, Diamond, and Gyroid have an average value of $\delta_{avg} = 0.25$, while Scherk's T.

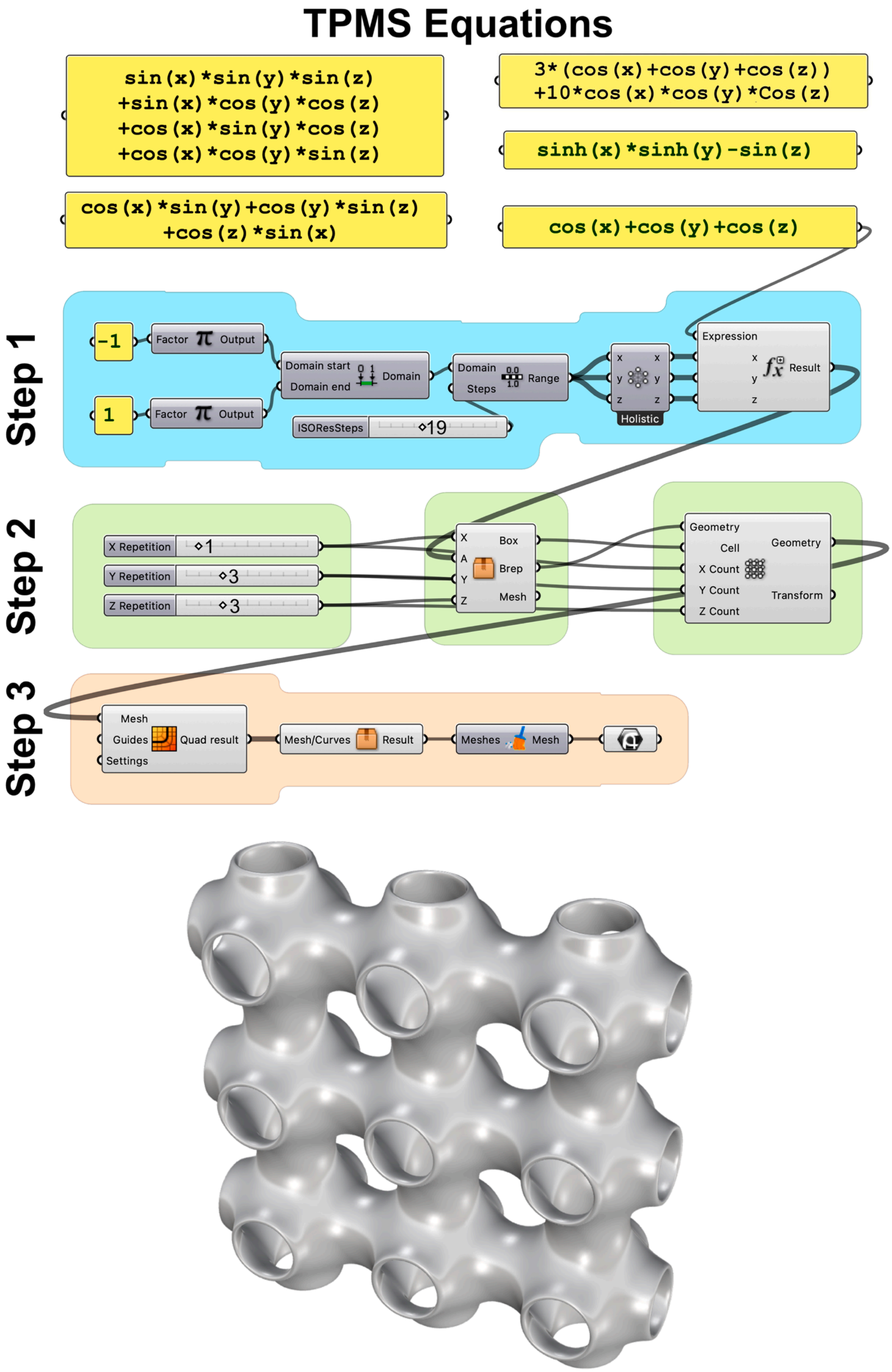

Fig. 2. Three-step workflow for TPMS generation (top), example of the TPMS generated surface (bottom).

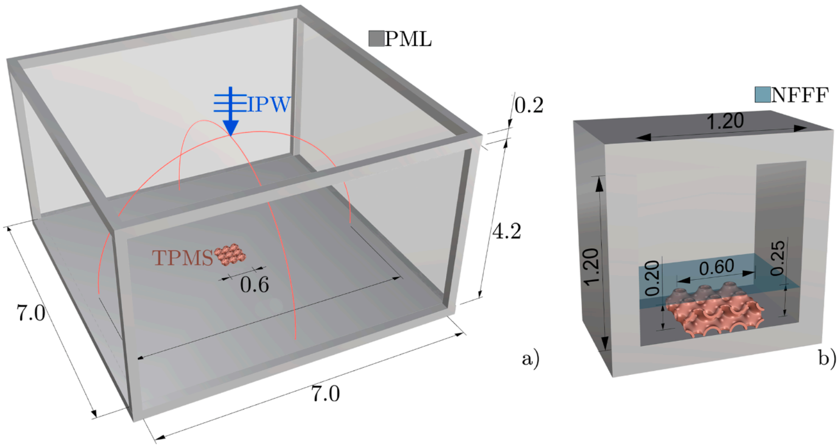

Fig. 3. 3D FDTD models used to calculate the diffusion coefficient δ. a) Big Model with the three-dimensional goniometer represented with the two red arcs. An acoustic Incident Plane Wave (IPW)is the excitation. b) NFFF model with the blue surface where the NFFF transform is made.All geometric dimension units are meters.

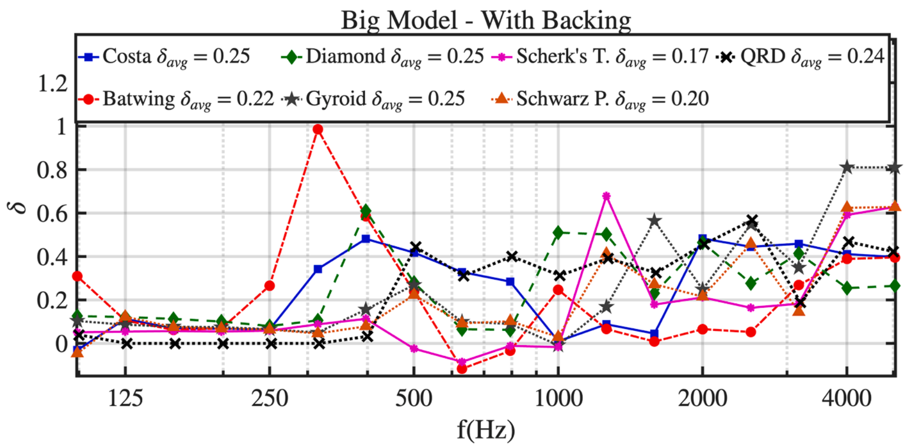

Fig. 4. Normalized diffusion coefficient (δ) with respect to a flat surface, evaluated using the big FDTD model with a rigid backing placed behind the TPMS. Also, experimental values of a QRD diffuser with the same depth (0.2 m) [11]. Different colors and markers are used to represent each TPMS. The average value of the normalized diffusion coefficient is indicated in the legend.

exhibits the lowest $\delta_{avg} = 0.17$. Nevertheless, spectral variations are observed in some cases. The Batwing TPMS shows large fluctuations in diffusion. At 315 Hz, a maximum value of $\delta = 1$ is observed, which then sharply drops, becoming worse than a flat surface at 630 Hz and 800 Hz. Scherk's T. also shows a pronounced diffusion peak at 1250 Hz, but in the 500–1000 Hz range it focuses the reflection, as indicated by negative values compared to the flat surface. The δ of the Gyroid increases steadily, reaching values above 0.8 at high frequencies (4000–5000 Hz). Scherk's T. surface maintains relatively low diffusion values across the frequency spectrum, with the exception of a distinct peak at 1250 Hz, while demonstrating focused reflection behavior in the 500–1000 Hz range. Finally, one of the most well-known geometries, Schwarz P., shows relatively consistent diffusion across the spectrum, surpassing $\delta = 0.6$ at 5000 Hz.

In the case of Fig. 4, the QRD values that have been experimentally measured in Cox's work [11] are given by a black line with cross-shaped markers. Since there is a large number of curves in the figure, it appears visually dense and a new comparative table (Table 2) has been added to help the reader. In this table, the values that are smaller than those for a flat surface are underlined whereas the values that are greater than the normalized QRD performance are highlighted in bold text. There are numerous inferences from this comparison. Primarily, TPMS structures indicate better diffusion performance concerning the QRD in the low-frequency bands of 125, 160, and 200 Hz, and also in the high-frequency bands defined by the standard, i.e., 4000 and 5000 Hz. In addition, it can be noted that, although a sharp diffusion peak for Scherk's T. can be seen near the 1250 Hz band, this structure has the worst sound diffusion performance overall. This finding corroborates the low average diffusion coefficient (0.17) of the Scherk'sT that has already been pointed out in the legend of Fig. 4.

Table 2
Normalized diffusion coefficient (δ) evaluated using the big FDTD model with a rigid backing placed behind the TPMS and experimental values of a QRD diffuser with the same depth (0.2 m) [11]. Values exceeding the QRD are shown in **bold**, while negative TPMS values are shown in underline.

f (Hz)	Costa	Batwing	Diamond	Gyroid	Scherk's T.	Schwarz P.	QRD
100	<u>-0.031</u>	**0.309**	**0.126**	**0.104**	**0.051**	<u>-0.046</u>	0.000
125	**0.113**	**0.105**	**0.122**	**0.086**	**0.054**	**0.123**	0.000
160	**0.070**	**0.062**	**0.113**	**0.077**	**0.057**	**0.075**	0.000
200	**0.068**	**0.069**	**0.101**	**0.075**	**0.054**	**0.069**	0.033
250	0.064	0.266	0.080	0.066	0.059	0.064	0.444
315	**0.343**	**0.986**	0.106	0.050	0.088	0.046	0.312
400	**0.481**	**0.586**	**0.611**	0.156	0.113	0.079	0.400
500	**0.418**	0.240	0.280	0.269	<u>-0.024</u>	0.223	0.313
630	0.329	<u>-0.116</u>	0.065	0.099	<u>-0.084</u>	0.092	0.391
800	0.285	<u>-0.034</u>	0.063	0.090	<u>-0.011</u>	0.102	0.325
1000	0.010	0.247	**0.510**	<u>-0.008</u>	<u>-0.017</u>	0.030	0.457
1250	0.088	0.066	0.502	0.169	**0.679**	0.412	0.567
1600	**0.245**	0.092	**0.493**	**0.221**	**0.451**	**0.272**	0.189
2000	0.426	0.275	**0.500**	0.339	0.249	0.215	0.468
2500	0.383	0.375	**0.457**	**0.449**	0.250	**0.458**	0.423
3150	0.412	0.409	0.394	0.560	0.145	0.625	0.000
4000	**0.413**	**0.460**	**0.398**	**0.715**	**0.628**	**0.628**	0.000
5000	**0.398**	**0.396**	**0.265**	**0.811**	**0.629**	**0.628**	0.000

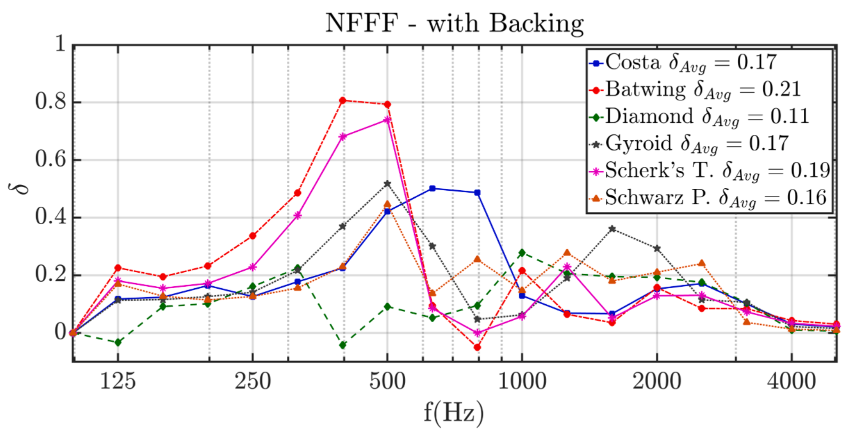

Fig. 5. Normalized diffusion coefficient (δ) with respect to a flat surface, evaluated using the NFFF FDTD model with a rigid backing placed behind the TPMS. Different colors and markers are used to represent each TPMS. The average value of the normalized diffusion coefficient is indicated in the legend.

Moreover, while Costa, Diamond, and Gyroid have the same average diffusion coefficient (0.25), Diamond is the only one that doesn't show any negative values. Therefore, it is the only TPMS that consistently has better performance than a flat surface throughout the analyzed frequency range.

Fig. 5 shows the results obtained with the NFFF model. While many peak values from the full-resolution model remain visible in the spectrum, all TPMS structures demonstrate δ values approaching 0 above 2000 Hz, effectively converging with flat surface performance. All average diffusion coefficients δ_{avg} are lower than those obtained with the full model, with Batwing standing out as the highest at 0.21, very close to the 0.22 obtained with the full model. The variations in all TPMS are smoother, exhibiting less abrupt curves, fewer sharp peaks, and more gradual changes across the evaluated frequency range.

The mean absolute error (MAE) between the reference "Big Model" and the low-computational cost model "NFFF" was computed for each TPMS geometry across the full frequency range (100–5000 Hz). The resulting per-geometry MAEs are as follows: **Costa**: 0.163, **Batwing**: 0.188, **Diamond**: 0.173, **Gyroid**: 0.208, **Scherk's T**: 0.247, **Schwarz P.**: 0.159. The overall MAE across all frequencies and geometries is: 0.190. Despite exhibiting an overall mean absolute error (MAE) of 0.2, the NFFF model achieves remarkably accurate approximations of the full-resolution simulation results across broad frequency ranges. This level of accuracy is particularly notable considering the dramatic reduction in computational cost: from 9.5 hours to 3 minutes, meaning that the NFFF takes only 0.53% of the time required by the big model. This performance demonstrates that the NFFF method is particularly well-suited for rapid parametric studies, preliminary design screening, and large-scale optimization problems, where moderate precision trade-offs are justified by substantial gains in computational efficiency.

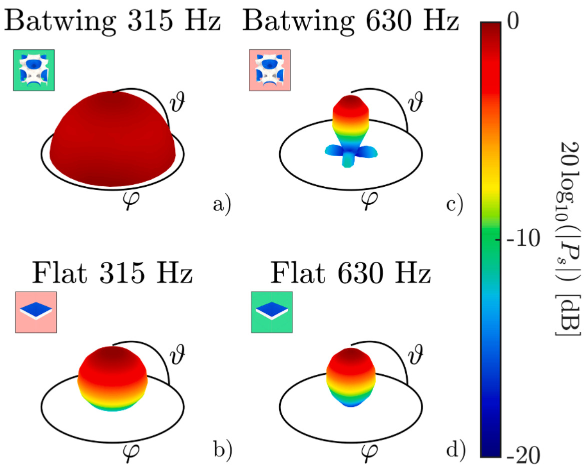

Fig. 6. Three-dimensional polar scattering patterns for the Batwing TPMS and a flat surface at 315 Hz and 630 Hz. At 315 Hz (a)the Batwing enhances diffusion with a nearly hemispherical pattern compared to the flat surface (b). At 630 Hz (c), the Batwing exhibits forward scattering and angular focusing, resulting in lower diffusion than the flat reference (d).

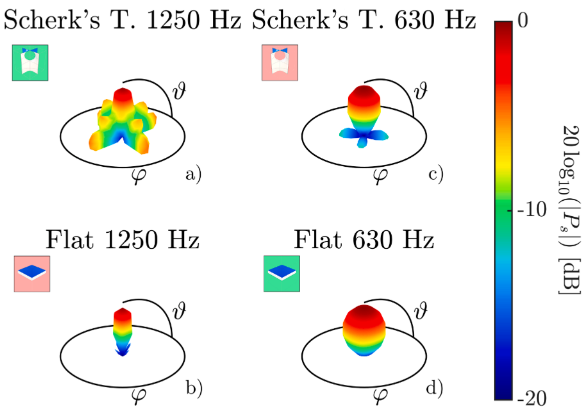

Fig. 7. Three-dimensional polar scattering patterns for the Scherk's T. TPMS and a flat surface at 1250 Hz and 630 Hz. At 1250 Hz (a), Scherk's T. shows enhanced diffusion with eight secondary lobes in orthogonal and diagonal directions, outperforming the flat surface (b). At 630 Hz (c), it exhibits angular focusing and reduced diffusion compared to the flat reference (d).

5.2. TPMS comparison analysis

In this subsection a comparison between each TPMS and a referenced flat surface is discussed. Figs. 6 through 11 present the optimal and suboptimal frequency ranges for acoustic diffusion performance by evaluating the scattered pressure fields in their three-dimensional polar patterns. The square insets displaying the unit cell represent the optimal and suboptimal cases for both flat surfaces and TPMS structures. Green colour shows when the TPMS has a high δ and red colour when the TPMS is focusing or when the flat surface is worst than the TPMS. Fig. 6 shows the three-dimensional polar scattering patterns for the Batwing TPMS and a flat surface at two representative frequencies: 315 Hz and 630 Hz. At 315 Hz (see Fig. 6a), which lies well below the Bragg frequency (f_{Bragg} = 857.5 Hz), the Batwing surface demonstrates enhanced diffusion compared to the flat reference (see Fig. 6b), resulting in a nearly uniform hemispherical distribution (with $\delta = 1$). By scaling the Batwing TPMS surface according to its lattice periodicity a and unit cell dimensions, the frequency at which maximum diffusion ($\delta = 1$) occurs can be tuned. Since the peak appears at 315 Hz for $a = 0.2$ m, the relationship $f_{Batwing\,MAX} = \frac{0.1837\,c}{a}$ shows that the diffusion peak depends on the periodicity. This means that adjusting a allows for direct control of the operating frequency, enabling application-specific tunability of the diffusive behavior. In contrast, at 630 Hz (see Fig. 6c), which approaches the Bragg regime but is still subwavelength with respect to the lattice constant, the Batwing exhibits strong forward scattering, indicating angular focusing rather than diffusion. This behavior leads to lower diffusion than the flat surface (see Fig. 6d) and produces a back-reflection acoustic focusing phenomenon.

Fig. 7 presents two representative frequencies for the Scherk's T. structure. At 1250 Hz (see Fig. 7 a and b), Scherk's T. exhibits superior diffusion compared to the flat surface, displaying a striking three-dimensional scattering pattern characterized by eight secondary lobes: four propagating along orthogonal directions in the azimuthal plane (ϕ), parallel to the surface, and four additional

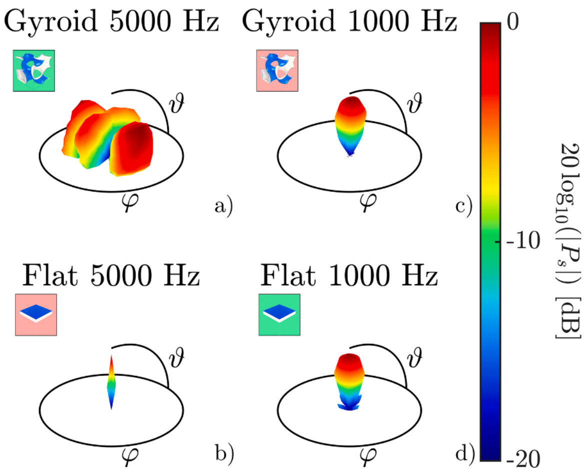

Fig. 8. Three-dimensional polar scattering patterns for the Gyroid TPMS and a flat surface at 5000 Hz and 1000 Hz. At 1000 Hz (c), the Gyroid begins to show angular spread compared to the directional flat reflection (d). At 5000 Hz (a), the Gyroid produces a rich multi-lobed diffusive pattern, while the flat surface (b) retains a narrow specular response.

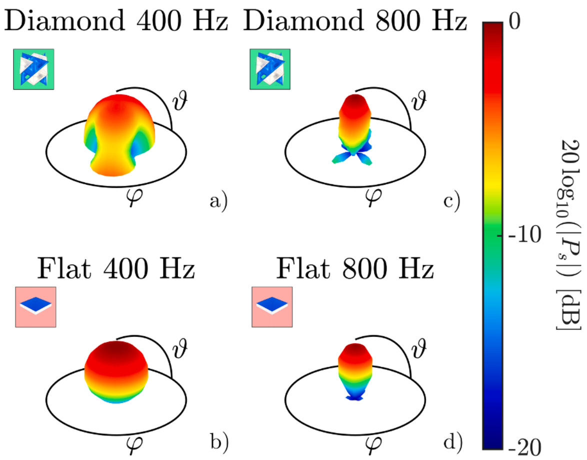

Fig. 9. Three-dimensional polar scattering patterns for the Diamond TPMS and a flat surface at 400 Hz(a,b) and 800 Hz(c,d). The Diamond shows superior diffusion in both cases, maintaining positive diffusion coefficients across the full frequency range analyzed.

lobes along diagonal directions at $\theta = 45°$. In contrast, at 630 Hz (see Fig. 7 c and d), Scherk's T. performs worse than the flat reference surface, showing slight specular reflection and angular focusing.

Fig. 8 displays the three-dimensional polar scattering patterns for the Gyroid TPMS and a flat surface at two different frequencies: 1000 Hz and 5000 Hz. At 1000 Hz (see Fig. 8c and d), both the Gyroid and the flat surface present relatively directional scattering patterns, though the Gyroid already exhibits signs of reduced diffusion in the lower blue part spread. The normalized diffusion coefficient δ of the Gyroid at 1000 Hz is only -0.008, which explains the visual similarity between its scattering pattern and that of the flat surface. In contrast, at 5000 Hz (see Fig. 8a and b), the Gyroid structure shows a highly complex and diffusive scattering pattern with multiple lobes distributed across a wide angular range. This significant diffusion enhancement contrasts markedly with the flat reference surface, which maintains a narrow, specular reflection pattern.

Diamond is the only TPMS that maintains positive normalized diffusion coefficients(δ) across the entire frequency range analyzed. Based on this behavior, and in contrast to other TPMS, Fig. 9 displays the two representative frequencies corresponding to its best (400 Hz) and worst (800 Hz) diffusion performance. Even at 800 Hz (see Fig. 9c), with more focused scattering pattern, the Diamond structure still outperforms the flat reference (see Fig. 9d), confirming its consistently diffusive nature across the spectrum.

Fig. 10 illustrates the three-dimensional angular diffusion behavior of the Schwarz P. compared to a flat reference at two representative frequencies. At 5000 Hz (see Fig. 10a and b), the Schwarz P. structure displays remarkable diffuse reflection, with a rich lobed pattern indicating multidirectional scattering across both azimuthal (φ) and polar (ϑ) angles. In contrast, the flat surface exhibits a narrow specular response concentrated at normal incidence, demonstrating limited diffusion capability. At 100 Hz (see Fig. 10c and d), both Schwarz P. and the flat panel exhibit similar nearly hemispherical scattering, dominated by specular reflection

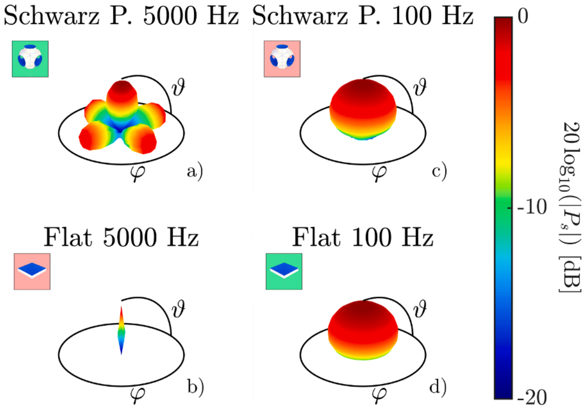

Fig. 10. Three-dimensional polar scattering patterns for the Schwarz P. TPMS and a flat surface at 5000 Hz (a,b) and 100 Hz (c,d). The Schwarz P. exhibits strong angular diffusion at high frequency, while both structures show comparable specular behavior at 100 Hz. (c) Schwarz P. is slightly worse with normalized diffusion coefficent ($\delta = -0.046$) compared with flat surface(d).

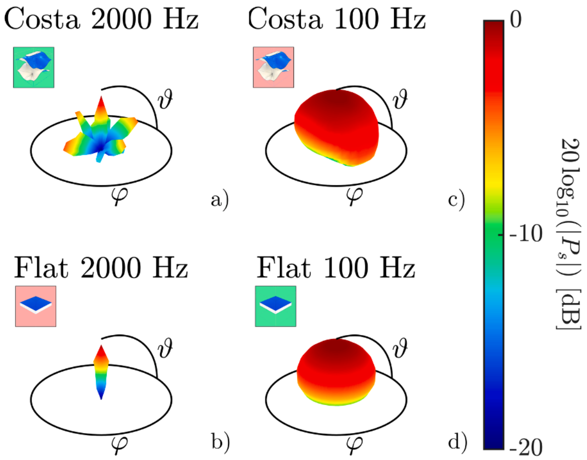

Fig. 11. Three-dimensional polar scattering patterns for the Costa TPMS and a flat surface at 2000 Hz (a,b) and 100 Hz (c,d). The Costa structure shows rich directional diffusion at high frequency, while both surfaces behave similarly at 100 Hz, dominated by specular reflection.

with minimal angular features. Schwarz P. (see Fig. 10c) has only -0.046 δ compared with the flat surface.These results highlight the frequency-dependent diffusive capabilities of the Schwarz P. TPMS.

Fig. 11 presents the angular scattering performance of the Costa TPMS compared to a flat surface at two representative frequencies. At 2000 Hz (see Fig. 11a and b), the Costa structure generates a complex three-dimensional scattering pattern, characterized by four prominent lobes oriented perpendicularly in the azimuthal plane (φ) and slightly tilted upward in the polar direction (ϑ). This multidirectional scattering clearly outperforms the flat surface, which exhibits a narrow specular response. At 100 Hz (see Fig. 11c and d), both the Costa and the flat surface show similar hemispherical profiles dominated by specular reflection and minimal angular diffusion. Costa TPMS has a -0.03 δ, which represent a small focalizacion compared with the flat reference.

6. Potential application: indoor acoustic partition panels

The design and evaluation of TPMS-based diffusive surfaces is not only of academic interest but also holds promise for real-world applications going further than already extended acoustic diffusers placed on walls. One new example is the development of *acoustic partition panels* (Fig. 12a), which are increasingly used in open-plan office environments to enhance speech clarity and reduce auditory distractions[59]. These lightweight and visually permeable structures can be optimized and scaled to scatter sound effectively within the vocal frequency range, particularly between 300 and 500 Hz, where speech intelligibility is most sensitive[60,61].

Our findings show that specific TPMS geometries exhibit strong frequency-dependent diffusion in this range, suggesting that their integration into architectural acoustic panels could contribute to improved acoustic comfort in shared workspaces. This opens a new avenue for combining functional performance with aesthetic design, leveraging the natural periodicity and three-dimensional complexity of TPMS. To obtain a more detailed analysis of the diffusive properties of each TPMS, we use the “Big model” without placing a rigid backing behind the structure, only a PML was used to simulate a non-reflective boundary, as if the structure were

Fig. 12. TPMS-based surfaces adapted designs to improve speech clarity. a) Schwarz P. acoustic partition panel used in office environments. b) Batwing TPMS diffuser with rigid backing on an office wall. c) Schwarz P. TPMS diffuser with rigid backing on an office wall.

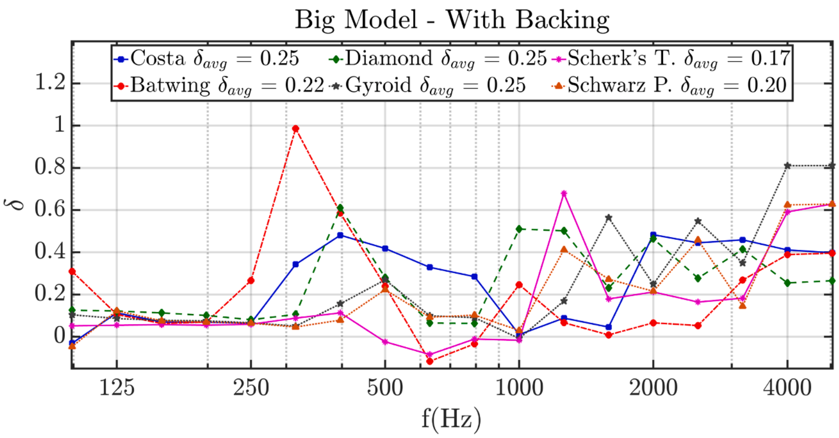

Fig. 13. Normalized diffusion coefficient (δ) with respect to a flat surface, evaluated using the big FDTD model without any backing behind the TPMS. Different colors and markers are used to represent each TPMS. The average value of the normalized diffusion coefficient is indicated in the legend.

placed directly in front of a wall that does not reflect sound. Fig. 13 shows the normalized diffusion coefficient δ for the TPMS without any rigid backing. At low frequencies (100–300 Hz), all surfaces exhibit relatively flat and low diffusion curves, indicating minimal angular scattering and limited frequency selectivity in this range. As the frequency increases, diffusion generally improves across all structures, although the enhancement and peaks are less pronounced than in the rigid-backed case depicted in Fig. 4. The Batwing structure still presents the most prominent peak in diffusion, now shifted from 315 Hz to 400 Hz, suggesting a change in resonant behavior in the absence of a backing layer. Meanwhile, Costa and Scherk's T. maintain superior performance in the mid- and high-frequency ranges, both reaching the highest average diffusion value of $\delta_{avg} = 0.27$. Diamond, Gyroid, and Schwarz P. follow with more moderate performance, particularly at higher frequencies. These results emphasize the influence of the backing condition on both the frequency response and diffusive efficiency of TPMS.

The presence of a rigid backing helps the diffusion behaviour of TPMS structures greatly. Because of the high contrast in acoustic impedance, the backing can be considered as almost a perfect reflector, which means that the transmission is very low. Acoustic waves going through the TPMS are reflected at the backing interface and meet the waves scattered by the structure, thus constructive and destructive interferences occur that determine the strong frequency-dependent sound diffusion response. On the other hand, if there is no backing, the transmitted waves are absorbed by the PMLs and only the direct scattering contribution of the TPMS is taken into account, which leads to overall smoother and lower sound diffusion.

7. Conclusion

In this study, we performed a detailed acoustic diffusion properties evaluation of six triply periodic minimal surfaces (TPMS), using two different three-dimensional FDTD simulation approaches aligned with ISO 17497-2. The results confirm the frequency-selective scattering behavior of TPMS and highlight their potential as efficient diffusive elements in architectural acoustics. The Batwing TPMS demonstrated a tunable diffusion peak around 315 Hz when backed by a rigid surface, which shifted to 400 Hz in the absence of backing, confirming its resonant nature. Other geometries like Costa and Scherk's Tower also exhibited strong diffusion in the mid-to-high frequency range. Diamond-shaped TPMS was the only one overpassing the sound diffusion performance of flat surface over the whole frequency range of 100–5000 Hz as stipulated in the ISO 17497-2 standard.

A comparison between full-domain simulations and the Near-Field to Far-Field (NFFF) model revealed a high correlation, with an average mean average error (MAE) of 0.19 and a computation time reduction of over 98%, making the later a compelling tool for acoustic diffusion, fast screening and optimization. Finally, the integration of TPMS in acoustic partition panels presents a promising application, particularly in the frequency range of 300–500 Hz, where Batwing's diffusion behaviour can enhance speech clarity and spatial sound distribution in shared indoor environments.

As a proposal for future continuation of this research, the numerical model framework will be extended to include elastic wave propagation within the TPMS material, to account for potential vibroacoustic effects in thin-walled sound diffusers. Moreover, psychoacoustic tests will be run to examine whether the perceptual enhancement caused by these diffusers results in a qualitative influence.

Data availability

The data that support the findings of this study are available from the corresponding author upon reasonable request.

CRediT authorship contribution statement

David Ramírez-Solana: Writing – original draft, Visualization, Validation, Software, Methodology, Investigation, Formal analysis, Data curation, Conceptualization; **Valentino Sangiorgio:** Writing – review & editing, Validation, Resources, Methodology, Investigation, Funding acquisition, Formal analysis, Data curation; **Javier Redondo:** Visualization, Validation, Software, Methodology, Investigation, Data curation, Conceptualization; **Muhammad Gulzari:** Writing – review & editing, Validation, Supervision, Resources, Project administration, Funding acquisition, Formal analysis, Data curation, Conceptualization.

Declaration of competing interest

The authors declare that they have no known competing financial interests or personal relationships that could have appeared to influence the work reported in this paper.

Acknowledgement

This research was supported by Construct Innovate, Ireland's National Research Centre for Construction Technology and Innovation (Enterprise Ireland TC-2022-0033, Seed Fund Call CISFC1-23_002). Also funding by grant PID2022-138321NB-C22 funded by MICIU/AEI/ 10.13039/501100011033 and ERDF/EU is acknowledged. We also acknowledge the support by project "MUD-MADE: MUlti-objective optimization of Digitally MAnufactureD Earth building components supported by neural networks (PRIN PNRR 2022)".

Appendix A. The costa surface

We define a periodic unit cell based on the Costa minimal surface, using the Gray parametrization scaled by a lattice constant a. As discovered by Gray and Ferguson [62,63], the Costa surface can be parametrically represented, see Eq. (A.1).

$$\begin{aligned} x &= a\,\Re\left(\zeta\left(u+\frac{\pi}{4e_1}\right)-\zeta(w)-\frac{1}{2}\zeta\left(w-\frac{i}{2}\right)\right),\\ y &= a\,\Re\left(\zeta\left(u+\frac{\pi}{4e_1}\right)-\zeta(w)+\frac{1}{2}\zeta\left(w-\frac{i}{2}\right)\right),\\ z &= a\sqrt{\frac{c}{e_1}}\ln\left|\frac{\wp(w)-e_1}{\wp(w)+e_1}\right|. \end{aligned} \tag{A.1}$$

where $w = u + iv$, with $u > 0, v \le 1$, and ζ refers to the Weierstrass zeta function (`WeierstrassZeta[z, {c, 0}]` in *Mathematica*). The function $\wp$ denotes the Weierstrass elliptic $\mathcal{P}$-function [54]. This function is also associated with the pair $(c, 0)$ (`WeierstrassP[z, {c, 0}]` in *Mathematica*).

The invariants of the Weierstrass functions correspond to the half-periods $\frac{1}{2}$ and $\frac{i}{2}$, and the first root is given by

$$e_1 = \wp\left(\frac{1}{2};0,g_3\right) = \wp\left(\frac{1}{2}\middle|\frac{1}{2},\frac{i}{2}\right) \approx 6.87519, \tag{A.2}$$

as listed in OEIS entry A133748 [64]. The values of the invariants are approximately $(g_2, g_3) = (189.072772\ldots, 0)$ (listed in OEIS entry A133747[65]). The constants c and $e_1 = \frac{\sqrt{c}}{4}$ are associated with the Weierstrass functions, with approximate values 189.7272…and 6.87519…, respectively.

Until 1982, it was conjectured that the only complete (i.e., without boundary), non-periodic minimal surfaces without self-intersections were the plane, the catenoid, and their associated surfaces. The discovery of Costa's surface disproved this conjecture.

The Costa surface can also be obtained via the classical Weierstrass parametrization of a minimal surface, by setting $f(z) = \wp(z)$ and $g(z) = \frac{-2\sqrt{2\pi e_1}}{\wp'(z)}$, leading to:

$$\begin{aligned} x &= \Re\left(\int_0^w \left(1 - g(z)^2\right) f(z)\, dz\right), \\ y &= \Re\left(-i\int_0^w \left(1 + g(z)^2\right) f(z)\, dz\right), \\ z &= \Re\left(2\int_0^w g(z) f(z)\, dz\right). \end{aligned} \tag{A.3}$$

To generate a solid structure with a physical thickness t, the surface is defined as the zero level set of a scalar field $\phi(x, y, z)$, constructed from the parametric representation. The corresponding solid shell is defined as the set of points satisfying:

$$|\phi(x, y, z)| \le \frac{t}{2}, \tag{A.4}$$

where $\phi(x, y, z)$ approximates the signed distance to the Costa surface.

References

[1] M.R. Schroeder, Diffuse sound reflection by maximum length sequences, J. Acoust. Soc. Am. 57 (1) (1975) 149–150. https://doi.org/10.1121/1.380437
[2] T.J. Cox, P. D'Antonio, Acoustic Absorbers and Diffusers, Taylor and Francis, New York, 2nd ed., 2009.
[3] T.J. Cox, Designing curved diffusers for performance spaces, Jo. Audio Eng. Soc. 44 (5) (1996) 354–364.
[4] M.R. Schroeder, Towards better acoustics for concert halls, Phys. Today 33 (6) (1980) 24–30. https://doi.org/10.1063/1.2914054
[5] J. Angus, Sound diffusers using reactive absorption grating, in: Proceedings of the 98th Convention of the Audio Engineering Society, Paris, 1995.
[6] R.J. Hughes, J.A.S. Angus, T.J. Cox, O. Umnova, G.A. Gehring, M. Pogson, D.M. Whittaker, Volumetric diffusers: pseudorandom cylinder arrays on a periodic lattice, J. Acoust. Soc. Am. 128 (5) (2010) 2847–2856. https://doi.org/10.1121/1.3493455
[7] J. Redondo, R. Picó, V. Sánchez-Morcillo, W. Woszczyk, et al., Sound diffusers based on sonic crystals, J. Acoust. Soc. Am. 134 (6) (2013) 4412–4417. https://doi.org/10.1121/1.4828826
[8] N. Jiménez, T.J. Cox, V. Romero-García, J.-P. Groby, et al., Metadiffusers: deep-subwavelength sound diffusers, Sci. Rep. 7 (1) (2017) 5389. https://doi.org/10.1038/s41598-017-05710-5
[9] L. Tan, J. Wu, J. Kang, H. Xu, et al., The visual preference and physiological response to sierpinski triangle acoustic diffuser: an experimental study using VR technique, J. Environ. Psychol. 93 (2024) 102227. https://doi.org/10.1016/j.jenvp.2023.102227
[10] M.R. Schroeder, Binaural dissimilarity and optimum ceilings for concert halls: more lateral sound diffusion, J. Acoust. Soc. Am. 65 (4) (1979) 958–963. https://doi.org/10.1121/1.382601
[11] T.J. Cox, Y.W. Lam, Prediction and evaluation of the scattering from quadratic residue diffusers, J. Acoust. Soc. Am. 95 (1) (1994) 297–305. https://doi.org/10.1121/1.408361
[12] E. Ballestero, Y. Meng, P. Sheng, V. Tournat, V. Romero-García, J.-P. Groby, et al., Transforming room acoustics with causality-driven dual-function passive metamaterials, Adv. Mater. Technol. (2025) 2402082. https://doi.org/10.1002/admt.202402082
[13] E. Brandão, E. Fernandez-Grande, C. Gaudeoso, S.A. Verburg, A. Richard, et al., Three-dimensional directivity measurement of acoustic diffusers using regularized holography and sound field separation, J. Acoust. Soc. Am. 158 (5) (2025) 3936–3948. https://doi.org/10.1121/10.0039893
[14] J. Redondo, J.V. Sánchez-Pérez, X. Blasco, J.M. Herrero, M. Vorländer, et al., Optimized sound diffusers based on sonic crystals using a multiobjective evolutionary algorithm, J. Acoust. Soc. Am. 139 (5) (2016) 2807–2814. https://doi.org/10.1121/1.4948580
[15] N. Jiménez, J.-P. Groby, V. Romero-García, et al., Spiral sound-diffusing metasurfaces based on holographic vortices, Sci. Rep. 11 (1) (2021) 10217. https://doi.org/10.1038/s41598-021-89487-8
[16] R. Patraquim, L. Godinho, P. Amado Mendes, Design and optimization of the sound diffusers using radial basis functions-Based shapes and genetic algorithms, J. Acoust. Soc. Am. 141 (5_Supplement) (2017) 3664–3664. https://doi.org/10.1121/1.4987939
[17] A.H. Schoen, Infinite Periodic Minimal Surfaces without Self-Intersections, 5541, National Aeronautics and Space Administration, 1970.
[18] V. Sangiorgio, F. Parisi, F. Fieni, N. Parisi, et al., The new boundaries of 3D-Printed clay bricks design: printability of complex internal geometries, Sustainability 14 (2) (2022) 598. https://doi.org/10.3390/su14020598
[19] K.B. Shingare, S. Alkunte, B. Li, A. Schiffer, I. Kinloch, K. Liao, Multifunctional TPMS-based interpenetrating phase composites: a comprehensive review of structure, properties, piezoelectricity and applications, Compos. Part C Open Access 17 (2025) 100596. https://doi.org/10.1016/j.jcomc.2025.100596
[20] X. Li, X. Wang, M. Zhao, Z. Li, et al., Lattice metamaterials as advanced airborne sound insulators, Phys. Rev. Appl. 24 (6) (2025) 060501. https://doi.org/10.1103/2w5x-vh9f
[21] K.Q. Tran, T.-D. Hoang, J. Lee, H. Nguyen-Xuan, et al., Three novel computational modeling frameworks of 3D-printed graphene platelets reinforced functionally graded triply periodic minimal surface (GPLR-FG-TPMS) plates, Appl. Math. Model. 126 (2024) 667–697. https://doi.org/10.1016/j.apm.2023.10.043
[22] L. Jian, J. He, G. Wen, Z.-P. Wang, J. Yang, Y.M. Xie, J. Liu, et al., Multifunctional TPMS-based metastructures, Int. J. Mech. Sci. 293 (2025) 110208. https://doi.org/10.1016/j.ijmecsci.2025.110208
[23] S.C. Kapfer, S.T. Hyde, K. Mecke, C.H. Arns, G.E. Schröder-Turk, et al., Minimal surface scaffold designs for tissue engineering, Biomaterials 32 (29) (2011) 6875–6882. https://doi.org/10.1016/j.biomaterials.2011.06.012
[24] D.J. Yoo, Porous scaffold design using the distance field and triply periodic minimal surface models, Biomaterials 32 (31) (2011) 7741–7754. https://doi.org/10.1016/j.biomaterials.2011.07.019
[25] A. Barakat, B. Sun, Controlling TPMS lattice deformation for enhanced convective heat transfer: a comparative study of diamond and gyroid structures, Int. Commun. Heat Mass Transf. 154 (2024) 107443. https://doi.org/10.1016/j.icheatmasstransfer.2024.107443
[26] S.V. Balabanov, A.I. Makogon, M.M. Sychov, M.V. Gravit, M.K. Kurakin, et al., Mechanical properties of 3D printed cellular structures with topology of triply periodic minimal surfaces, Mater. Today. Proc. 30 (2020) 439–442. https://doi.org/10.1016/j.matpr.2019.12.392
[27] L. Doyle, H. Terrones, C. González, et al., On the rigidity and mechanical behavior of triply periodic minimal surfaces-based lattices: insights from extensive experiments and simulations, Adv. Eng. Mater. (2025) 2402495. https://doi.org/10.1002/adem.202402495
[28] F. Hesselmann, M. Halwes, P. Bongartz, M. Wessling, C. Cornelissen, T. Schmitz-Rode, U. Steinseifer, S.V. Jansen, J. Arens, et al., TPMS-Based membrane lung with locally-modified permeabilities for optimal flow distribution, Sci. Rep. 12 (1) (2022) 7160. https://doi.org/10.1038/s41598-022-11175-y
[29] D.W. Abueidda, I. Jasiuk, N.A. Sobh, et al., Acoustic band gaps and elastic stiffness of PMMA cellular solids based on triply periodic minimal surfaces, Mater. Des. 145 (2018) 20–27. https://doi.org/10.1016/j.matdes.2018.02.032
[30] X. Guan, E. Deckers, H. Dong, M. Hornikx, J. Yang, et al., Optimization of graded porous acoustic absorbers based on triply periodic minimal surfaces, Mater. Des. 253 (2025) 113852. https://doi.org/10.1016/j.matdes.2025.113852

[31] Y. Guo, M.I.N. Rosa, M. Ruzzene, et al., Topological surface states in a gyroid acoustic crystal, Adv. Sci. 10 (6) (2023) 2205723. https://doi.org/10.1002/advs.202205723
[32] J.-Y. Lu, T. Silva, F. Alzaabi, R.K. Abu Al-Rub, D.-W. Lee, et al., Insights into acoustic properties of seven selected triply periodic minimal surfaces-based structures: a numerical study, J. Low Freq. Noise Vibr. Active. Contr. 43 (1) (2024) 208–219. https://doi.org/10.1177/14613484231190986
[33] K.K. Sirivuri, V. Sekar, W.J. Cantwell, K. Liao, B. Berton, N. Ravaud, P.-M. Jacquart, R.K. Abu Al-Rub, et al., Computational study of sound absorption in TPMS lattice materials using a thermoviscous model, J. Build. Eng. 112 (2025) 113658. https://doi.org/10.1016/j.jobe.2025.113658
[34] V.-L. Nguyen, J. Rungamornrat, Free vibration analysis of rotating functionally graded triply periodic minimal surface cylindrical shells, Mater. Emerging Technol. Sustain. 01 (03) (2025) 2550013. https://doi.org/10.1142/S306093212550013X
[35] J.G. Maloney, K.E. Cummings, Adaption of FDTD techniques to acoustic modelling, 11th Annual Review of Progress in Applied Computational Electromagnetics 2 (1995) 724–731.
[36] A. Taflove, S.C. Hagness, M. Piket-May, Computational electromagnetics: the finite-difference time-domain method, in: The Electrical Engineering Handbook, Elsevier, 2005, pp. 629–670. https://doi.org/10.1016/B978-012170960-0/50046-3
[37] J. Redondo, R. Picó, B. Roig, M.R. Avis, Time domain simulation of sound diffusers using finite-Difference schemes, Acta Acust. United Acust. 93 (2007) 611–622.
[38] J.-P. Berenger, A perfectly matched layer for the absorption of electromagnetic waves, J. Comput. Phys. 114 (2) (1994) 185–200. https://doi.org/10.1006/jcph.1994.1159
[39] D.A. Hoffman, W.H. Meeks, A complete embedded minimal surface in $\mathbb{R}^3$ with genus one and three ends, J. Differ. Geom. 21 (1) (1985). https://doi.org/10.4310/jdg/1214439467
[40] D. Hoffman, W.H. Meeks, Limits of minimal surfaces and scherk's fifth surface, Arch. Ration. Mech. Anal. 111 (2) (1990) 181–195. https://doi.org/10.1007/BF00375407
[41] W.H. Meeks, The conformal structure and geometry of triply periodic minimal surfaces in $\mathbb{R}^3$, Bull. Am. Math. Soc. 83 (1) (1977) 134–136. https://doi.org/10.1090/S0002-9904-1977-14218-3
[42] V.R. Batista, A family of triply periodic costa surfaces, Pac. J. Math. 212 (2) (2003) 347–370. https://doi.org/10.2140/pjm.2003.212.347
[43] C. Costa, Imersões Mínimas Em $\mathbb{R}^3$ de Gênero Um e Curvatura Total Finita, Ph.D. thesis, IMPA, Rio de Janeiro, Brasil, 1982.
[44] Y. Shi, P. Wang, X. Wang, et al., Conjugate surfaces of a family of minimal surfaces of genus 1 with 4 planar ends in $\mathbb{R}^3$, Chin. Ann. Math. Ser. B 45 (6) (2024) 927–942. https://doi.org/10.1007/s11401-024-0045-1
[45] X. Yuan, D. Borup, J.W. Wiskin, M. Berggren, S. Johnson, Formulation and validation of berenger's PML absorbing boundary for the FDTD simulation of acoustic scattering, IEEE Trans. Ultrason. Ferroelectr. Freq. Contr. 44 (4) (1997) 816–822. https://doi.org/10.1109/58.655639
[46] A. Bermúdez, L. Hervella–Nieto, A. Prieto, R. Rodríguez, Perfectly matched layers, in: S. Marburg, B. Nolte (Eds.), Computational Acoustics of Noise Propagation in Fluids - Finite and Boundary Element Methods, Springer Berlin Heidelberg, Berlin, Heidelberg, 2008, pp. 167–196. https://doi.org/10.1007/978-3-540-77448-8_7
[47] J.B. Schneider, C.L. Wagner, S.L. Broschat, Implementation of transparent sources embedded in acoustic finite-difference time-domain grids, J. Acoust. Soc. Am. 103 (1) (1998) 136–142. https://doi.org/10.1121/1.421084
[48] N. Ricker, Wavelet contraction, wavelet expansion, and the control of seismic resolution, Geophysics 18 (1953) 769–792. https://doi.org/10.1190/1.1437927
[49] A. Farina, A new method for measuring the scattering coefficient and the diffusion coefficient of panels, Acta Acust. United Acust. 86 (6) (2000) 928–942. Available on ResearchGate.
[50] M. Vorländer, E. Mommertz, Definition and measurement of random-incidence scattering coefficients, Appl. Acoust. 60 (2000) 187–199. https://doi.org/10.1016/S0003-682X(99)00051-1
[51] R.C. Johnson, H.A. Ecker, J.S. Hollis, Determination of far-field antenna patterns from near-field measurements, Proc. IEEE 61 (12) (1973) 1668–1694. https://doi.org/10.1109/PROC.1973.9322
[52] A.D. Yaghjian, An overview of near-field antenna measurements, IEEE Trans. Antennas Propag. 34 (1) (1986) 30–45. https://doi.org/10.1109/TAP.1986.1143800
[53] The MathWorks Inc., MATLAB Engine API for Python, 2024, (The MathWorks, Inc.).
[54] I. Moiseev, B. Carcich, Elliptic Functions for Matlab and Octave (Elliptic v1.0), 2008, (Zenodo). https://doi.org/10.5281/ZENODO.48264
[55] Robert McNeel & Associates, Rhinoceros 3D, 2025. https://www.rhino3d.com/
[56] International Organization for Standardization, ISO 17497-2 - Sound-scattering Properties of Surfaces. Part 2, Measurement of the Directional Diffusion Coefficient in a Free Field, 2012.
[57] P. D'Antonio, Design of a new testing chamber to determine the absorption, diffusion and scattering coefficients, in: PROCEEDINGS of the 23rd International Congress on Acoustics, Aachen (Germany), 2019.
[58] D. Ramírez-Solana, V. Sangiorgio, R. Picó, J. Redondo, Acoustic switch based on rotatable sonic crystal with multiresonant scatterers, Appl. Acoust. 240 (110913) (2025). https://doi.org/10.1016/j.apacoust.2025.110913
[59] G. Fratoni, M. Tenpierik, M. Turrin, M. Garai, D. D'Orazio, Acoustic performance of multi-resonator screens in a virtually reconstructed open-plan office, Appl. Acoust. 229 (2025) 110381. https://doi.org/10.1016/j.apacoust.2024.110381
[60] I.R. Titze, Physiologic and acoustic differences between male and female voices, J. Acoust. Soc. Am. 85 (4) (1989) 1699–1707. https://doi.org/10.1121/1.397959
[61] T.F. Cleveland, Acoustic properties of voice timbre types and their influence on voice classification, J. Acoust. Soc. Am. 61 (6) (1977) 1622–1629. https://doi.org/10.1121/1.381438
[62] H. Ferguson, A. Gray, S. Markvorsen, Costa's minimal surface via mathematica, Math. Educ. Res. 5 (1) (1996) 5–10.
[63] A. Gray, Costa'S minimal surface, in: Modern Differential Geometry of Curves and Surfaces with Mathematica, CRC Press, Boca Raton, FL, 2nd ed., 1997, pp. 747–757.
[64] The OEIS Foundation Inc., Sequence A133748 in the on-line encyclopedia of integer sequences, 2025. https://oeis.org/A133748
[65] The OEIS Foundation Inc., Sequence A133747 in the on-line encyclopedia of integer sequences, 2025. https://oeis.org/A133747